Light Water Reactor Sustainability Program

Applying grain-boundary sensitive electrochemical scanning probe techniques to evaluate intergranular degradation of irradiated and deformed stainless steels

September 2023

U.S. Department of Energy
Office of Nuclear Energy

Applying grain-boundary sensitive electrochemical scanning probe techniques to evaluate intergranular degradation of irradiated and deformed stainless steels

Ashutosh Jangde ([1]), Xin Chen ([1]), Maxim Gussev ([2]), Gaurav Sant ([1])

[1] University of California, Los Angeles, CA, USA
[2] Oak Ridge National Laboratory, Oak Ridge, TN, USA

September 2023

Prepared for the
U.S. Department of Energy
Office of Nuclear Energy

EXECUTIVE SUMMARY

Overview: In nuclear power plants, irradiation assisted stress corrosion cracking (IASCC) of the critical structural components can cause frequent shutdown of the nuclear reactor. This results in the power generation loss and incurring high maintenance cost. IASCC is a complex problem where the synergetic effect of irradiation, mechanical load, and corrosion activity all comes into play, thereby making its mechanism difficult to understand. Irradiation assisted elemental segregation (e.g., Cr-depletion at grain boundaries) can be the major reasons to induce IASCC, but the corrosion activity related to such compositional heterogeneities has not been fully understood. Thus, in present study, we address the effect of ion irradiation on the electrochemical corrosion over the localized features such as grain interiors, grain boundaries, and dislocation channels.

Implications: Our approach improves understanding the impact of irradiation assisted elemental segregation on the electrochemical corrosion of light water reactors' structural materials. The present work develops methodologies that can capture the subtle differences in the electrochemical behavior at the nanoscale, and therefore can be used to detect grain boundary corrosion susceptibilities of irradiated and deformed nuclear components.

ACKNOWLEDGEMENTS

The authors acknowledge financial support for this research from the U.S. Department of Energy's Light Water Reactor Sustainability (LWRS) Program Materials Research Pathway (MRP) through the Oak Ridge National Laboratory operated by UT-Battelle LLC (Contract #: 4000154999). The contents of this paper reflect the views and opinions of the authors who are responsible for the accuracy of data presented. This research was carried out in the institute for carbon management (ICM), University of California, Los Angeles (UCLA). As such, the authors gratefully acknowledge the support that has made these facilities and their operations possible. The authors acknowledge Dr. Marta Pozuelo for her help with gathering and analyzing transmission electron microscopy (TEM) data.

Contents

LIST OF FIGURES

LIST OF TABLES

Applying grain-boundary sensitive electrochemical scanning probe techniques to evaluate intergranular degradation of irradiated and deformed stainless steels

1. Introduction

Light water reactors (LWRs) often encounter the issue of irradiation-assisted stress corrosion cracking (IASCC), a well-known problem in nuclear energy industries. IASCC of the aging core structural materials (e.g., austenitic stainless steels) can result in catastrophic failure[1–3].To prevent such failure, a proper understanding of IASCC initiation and its propagation mechanism is vital so that unexpected shutdown or accident of LWRs can be eliminated. It has been understood that, the radiation induced segregation (RIS) at the grain boundaries is one of the major causes of IASCC[3]. Dislocation channeling resulted from the localized plastic deformation are also considered to promote IASCC, because of the surface step formation results in the rupture of passivating film and thereby cause localized corrosion[4]. However, the impact of RIS on the electrochemical corrosion remains unclear for nuclear materials. Thus, herein, the electrochemical characterizations over grain interiors and grain boundaries were attempted, the effect of RIS on the corrosion properties of different microstructural features were studied and quantified.

2. Experimental

2.1 Material

Herein, solution annealed austenitic stainless steel (304L and 316 L grades) having nominal chemical compositions, as shown in

Table *1*, was machined as the micro tensile sample with dimensions as shown in **Figure 1**(a). The materials with their form and condition are given in **Table 2**. This material is used for the electrochemical characterization at localized regions, i.e., grain interiors (GIs) and grain boundary (GBs). Prior to the electrochemical tests the samples were gently polished with colloidal silica (50 nm) and then subsequently rinsed with deionized water and then ultrasonically cleaned in fresh Isopropyl alcohol solvent.

Table 1. The chemical composition of the 304L and 316L stainless steel used (wt.%).

Sample/ elements	Fe	Cr	Ni	Mo	Mn	N	C	Si
304 L SS	bal.	18.29	8.02	0.07	1.28	0.05	0.02	0.45
316L SS	bal.	16.60	9.88	2.25	1.12	0.02	0.05	0.68

Table 2 Materials with their forms & conditions used this present investigation.

Sample	Materials and its form	Condition
1	304 L SS; Cylindrical disc	Sensitized at 675 °C for 24 hours
2	304 L SS; Micro tensile sample	Fe^{++} irradiated (5-dpa flat region) at 300 °C using 6 MeV [Fe^{++}] to a target fluence of 2×10^{16} ions/cm^2
3	316 L SS; Micro tensile sample	Ni^{++} irradiated (2-dpa flat region) at 300 °C and subsequently mechanically strained to fracture

2.2 Microstructural characterization

A Nova 600 SEM/FIB system was used to prepare electron transparent cross-sectional lamella for transmission electron microscopy (TEM) sample preparation. A FEI Titan 300KV scanning transmission electron microscope (STEM) equipped with an Oxford Instruments EDS system was used for microstructural and elemental analysis.

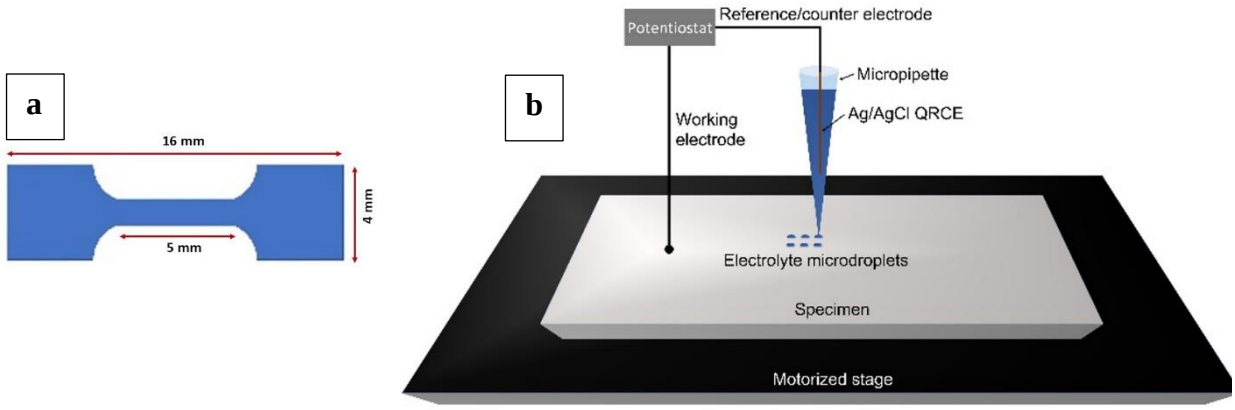

Figure 1. Schematic (a) of the tensile sample whose gauge length region irradiated with the Fe++ ions and (b) of scanning electrochemical cell microscopy used for localized electrochemical characterization.

Surface topography revealing the grain interiors and grain boundaries (due to the height difference in order of tens of nanometer) of irradiated sample were characterized with the help of vertical scanning interferometry (Zygo NewView 8200) instrument (VSI). VSI was also used to measure the size of the corrosive electrolyte micro-droplets immediately after electrochemical studies. The raw data captured by VSI was processed and analyzed by Gwyddion-2.62 software.

Scanning Kelvin probe force microscopy (SKPFM), an Atomic Force Microscopy (AFM) based technique, is used to characterize the surface potential. For this AFM instrument, Bruker Dimension Icon SPM with the AFM probe made of silicon tip on silicon cantilever (PFQNE-AL) was utilized. The SKPFM was operated in PeakForce

mode with two pass processes. The first pass measured the topography and then surface potential was measured during the second pass. Lift height of 25 nm was used for the potential measurements.

2.3 Electrochemical characterization

The electrochemical characterization at the localized region was carried out by utilizing the scanning electrochemical cell microscopy (SECM) setup (HEKA ElProScan). Schematic picture of SECM set up is shown in **Figure 1**(b). Herein, the corrosive electrolyte used was the aqueous solution with composition of 20 mM LiCl + 5% HNO_3. Herein, LiCl was used as potential cooling contaminant promoting measurable corrosion current whereas HNO_3 was used to dissolve the surface hydroxide layer and thereby revealing the corrosion resistance of only the barrier oxide layer. Deionized (DI) water with an electrical conductivity approximately around 18 MΩ-cm^2 was used to make the aqueous corrosive electrolyte. The electrochemical cell was operated in the two-electrode mode namely working electrode (WE) and quasi-reference-counter-electrode (QRCE). The irradiated sample acts WE while the AgCl coated Ag wire immersed in the corrosive electrolyte filled micro probe (with < 2 µm tip opening diameter) acts as the QRCE. Herein onwards all the potential are with respect to the Ag/AgCl QRCE. After QRCE approached the sample, the electrochemical characterizations were carried out. Open circuit potentials (OCPs) were measured for the duration of 60 seconds. Electrochemical impedance spectroscopy test was carried out at OCP utilizing 10 mV as a stimulus signal over the frequency range from 10^4 to 10^0 Hz whereas the potentiodynamic polarization test were conducted at the 10 mV/s scan rate from -250 mV (cathodic range) with respect to OCP to +250 mV (anodic range). All the electrochemical tests were carried out in ambient conditions.

3. Results and Discussions

3.1 STEM/TEM study of Fe^{++} ion irradiated 304L stainless steel

Our pathway to reveal RIS and the resulted grain boundary corrosion activities was to first characterize RIS at/near grain boundaries using microstructural analysis. **Figure 2** depicting the high-angle annular dark-field (HAADF) scanning transmission image depicting the grain and grain boundary structure. The EDS mapping (for Fe, Cr, Ni, & O elements) in the region with grain boundary and its adjoining structure is also shown in the colored picture in the **Figure 2**. It was observed that the spatial elemental distribution of Fe and Cr were not uniform along the grain boundary. The observed Cr depletion along the GB is possibly due to the Fe^{++} ion irradiation, this observation is consistent with the literature findings of irradiation damages in stainless steels as reported by Rajan et. al[5] and Fukuya et. al[6].

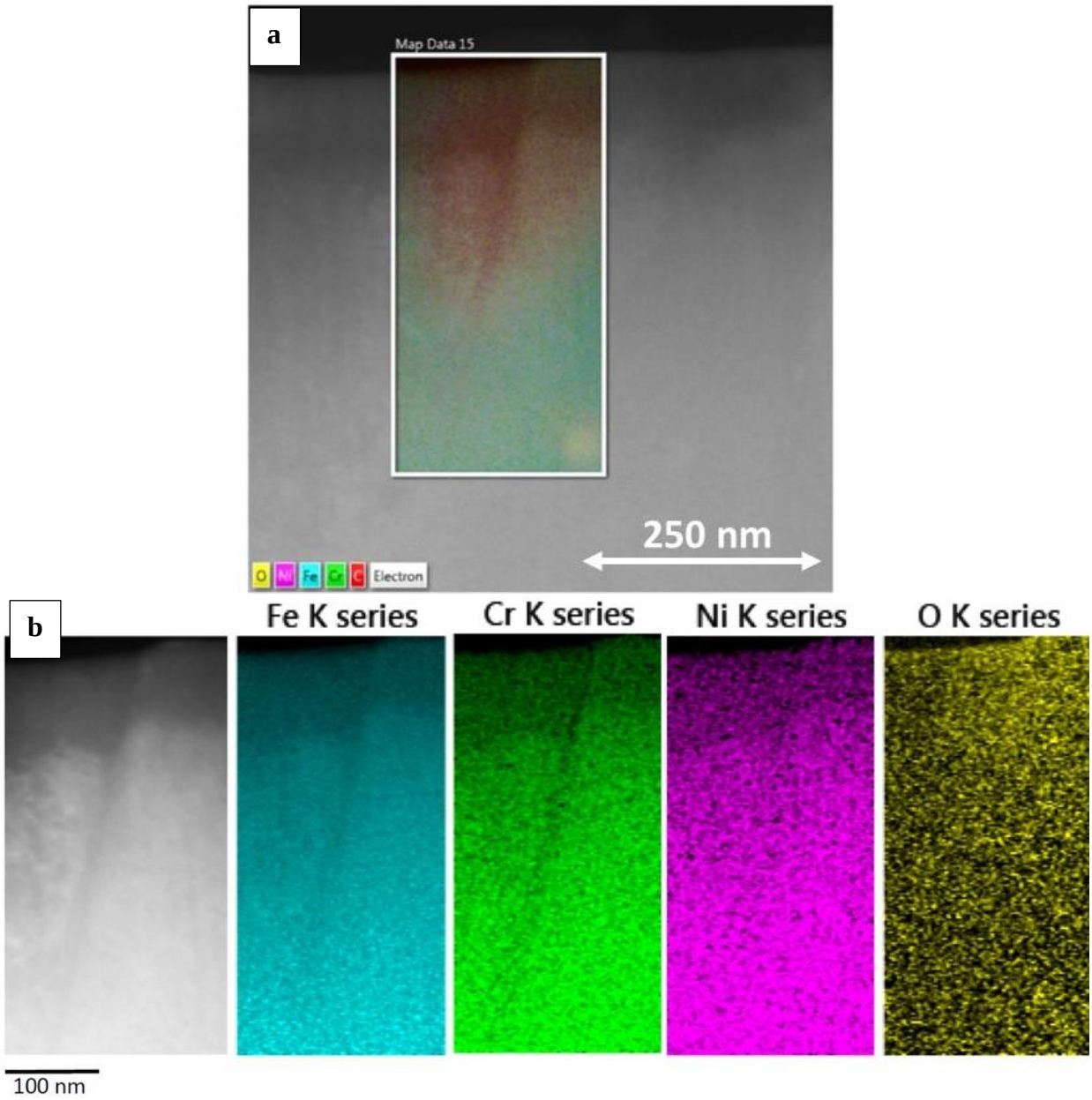

Figure 2 (a) High-angle annular dark-field (HAADF) scanning transmission image and (b) its corresponding EDS mapping of the grain boundary and its adjacent grains revealing spatial distribution of Fe, Cr, Ni, & O elements for the Fe^{++} ion irradiated 304L stainless steel.

High resolution TEM analysis not only revealed the highly defective grain boundary, but also disclosed the presence of ferrite phases at the grain boundary between the austenite phases as shown in **Figure 3**. Similarly, irradiation induced ferrite formation was previously reported by Porter[7] and Stanley et al[8]. The TEM and HRTEM images are given in **Figure 3** (a & b) respectively. The fast fourier transform (FFT) of the squared region (in **Figure 3**(b)) are show in **Figure 3**(c) showing the presence of austenite (fcc) and ferrite phases (bcc) with the $(01\text{-}1)_{bcc}//(11\text{-}1)_{fcc}$ orientation relationship.

Additionally, Fe-Cr rich oxide ($FeCr_2O_4$) was also observed at the grain boundary between the austenite grains as depicted in **Figure 3** (d & e) suggesting grain boundary oxidation. These observations are also consistent with the literature reports of irradiated stainless steel by Boisson et al.[9] and Terachi et al.[10].The inset image in **Figure 3**(e) illustrates an indexed FFT confirming the presence of $FeCr_2O_4$ (in yellow) in addition to the α-ferrite phase oriented to [-111] zone axis.

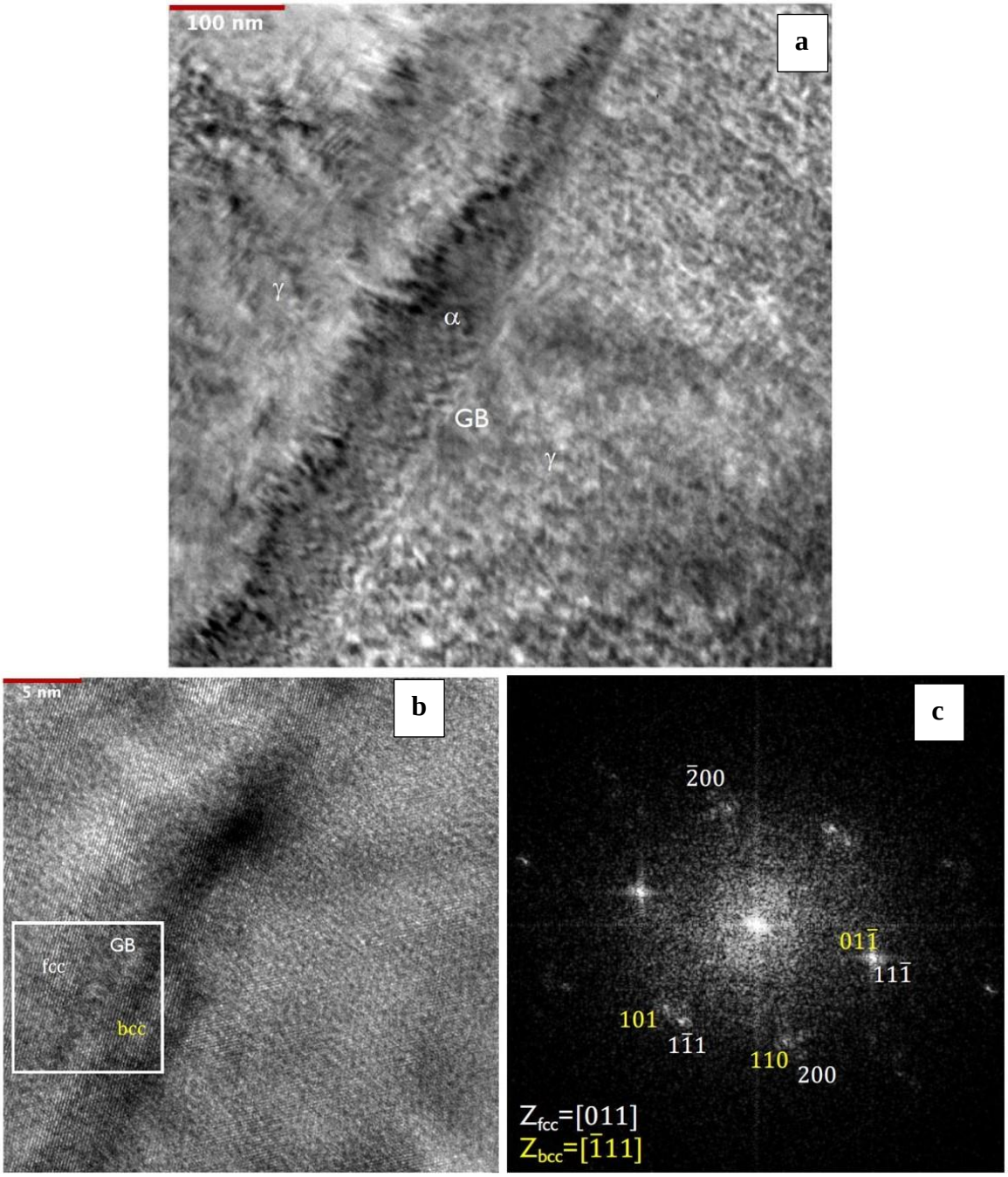

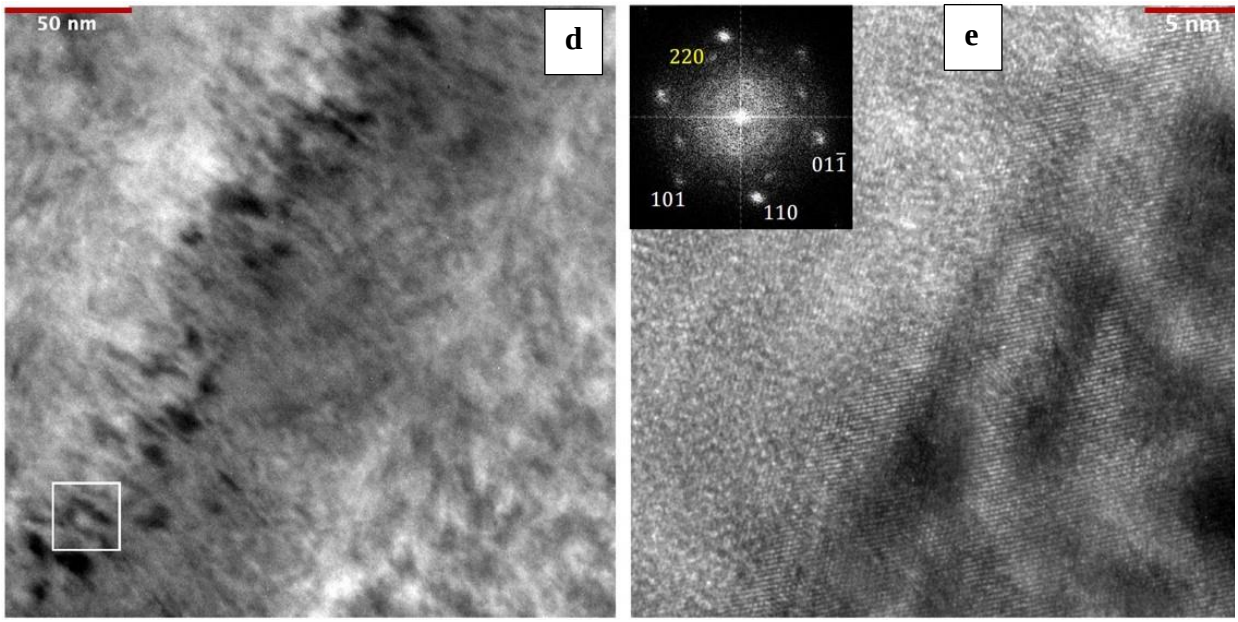

Figure 3 (a) TEM image showing a α-ferrite precipitate at the grain boundary between two γ-austenite grains; (b) HRTEM image depicting the lattice fringes of bcc phase (α-ferrite) and fcc phase (γ-austenite); (c) showing the FFT of the squared region of (b); (d) is TEM image showing γ-austenite grains on either side of grain boundary and the squared region are presented in HRTEM image in (e). The inset image in (e) illustrates an indexed FFT confirming the presence of $FeCr_2O_4$ (in yellow) in addition to the α-ferrite phase oriented to [-111] zone axis.

3.2 Localized electrochemical characterization of sensitized 304L stainless steel

Prior to performing corrosion analysis with limited quantity of ion-irradiated samples, we simulated the Cr-depletion at grain boundaries by sensitizing the 304L stainless steel at 675 °C for 24 hours. This sensitized stainless steel acts as a surrogate for the irradiated samples. Conveniently, grain boundaries can be disclosed by topographical maps of the polished 304L stainless steel, simply due to the different surface retreat of the grains with different orientations. **Figure 4**(a) showing the VSI image with the topography feature revealing grain interior and grain boundary regions, and the same area is shown in **Figure 4**(b) indicate where the SECM's micro probe was landed to perform the electrochemical characterization. **Figure 4**(c) shows the Nyquist plot illustrating relatively higher impedance for GI than for GB of the sensitized 304L stainless steel. Higher impedance indicates better corrosion resistance[11].

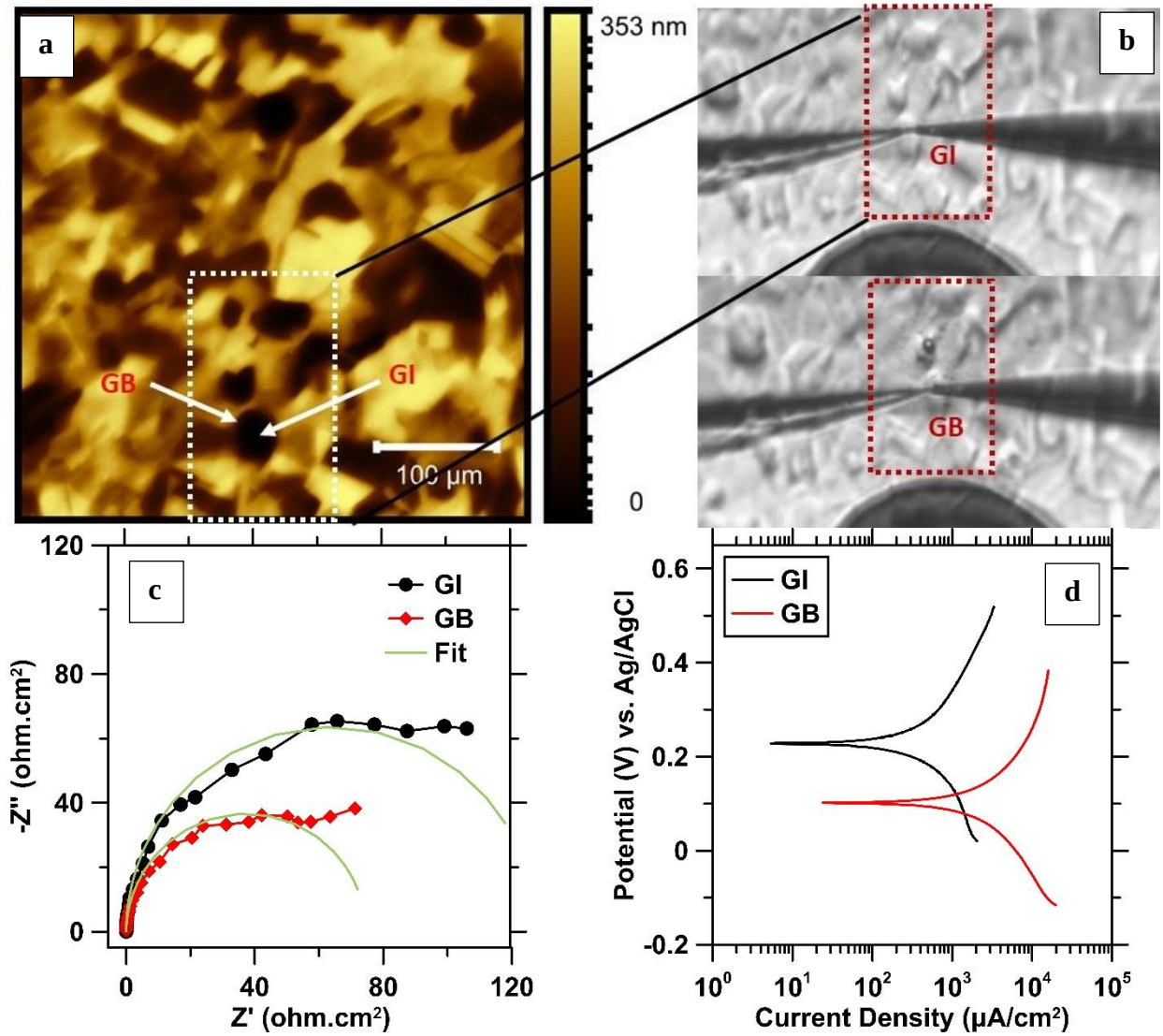

Figure 4 VSI image (a) showing the region of grain interior (GI) and grain boundary (GB) over which micro probe attached with the SECM are placed as depicted in (b) for the electrochemical impedance spectroscopy (EIS) and potentiodynamic polarization tests of sensitized 304L stainless steel.

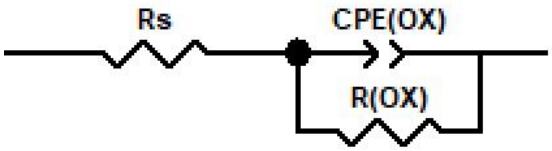

Figure 5 Electrochemical equivalent circuit used for modelling the EIS spectra over GB and GI.

EIS spectra were modeled with the electrochemical equivalent circuit (EEC) shown in **Figure 5**. In the electrochemical equivalent circuit, constant phase element (CPE) is used to represent heterogeneity in the electrode system[12] and its impedance is mathematically given by the Equation as follows:

$$Z_{CPE} = \frac{1}{T(j\omega)^{\alpha}};\ -1 \leq \alpha < 1$$

where T is the CPE coefficient, α is CPE index, j=complex unit to define imaginary number; j = 1, ω = angular frequency (which is related to frequency, f, as ω=2πf). The dispersion of electrode system due to the heterogeneity such as rough surface, porous surface, etc. can be accounted by the CPE index, α, which can vary in the range of -1 ≤ α≤1. CPE simulates as an ideal capacitor, an ideal inductor, and an ideal resistor when it is equal to 1, -1, and 0 respectively[13]. R_s represents the electrolyte solution resistance; $CPE_{(OX)}$ represents capacitance of passivating oxide film; and $R_{(OX)}$ represents the resistance of passivating oxide film. The value extracted from EIS spectra fitting is listed in **Table 3**. from which it was observed that the resistance offered by the oxide layer over GI was relatively higher than over GB indicative of higher corrosion resistance of the former.

Table 3 EEC element values from the EIS spectra fitting of GI and GB of sensitized 304L stainless steel.

Region/EEC element	R_s (ohm.cm^2)	$CPE_{(OX)}$-T (Ω^{-1} cm^{-2}s$^{\alpha}$)	$CPE_{(OX)}$-α	$R_{(OX)}$ (ohm.cm^2)
GI	(2.4 ± 2.7) × 10^{-3}	(3.6 ± 0.2) × 10^{-4}	0.997 ± 0.006	127.7 ± 4.7
GB	(1.4 ± 3.3) × 10^{-3}	(4.0 ± 0.2) × 10^{-4}	0.987 ± 0.008	74.7 ± 2.9

Potentiodynamic polarization curve over GI and GB of the sensitized 304L stainless steel in **Figure 4**(d) and the corrosion properties obtained from its Tafel fitting are given in **Table 4**. The corrosion potential, E_{corr}, was relatively lower at GB than of GI, and the corrosion current density, i_{corr}, was relatively higher at GB. Corrosion potential, E_{corr}, is a thermodynamic corrosion property indicating the tendency to corrode. As an acid electrolyte was used in the corrosion analysis, hydrogen evolution reaction (HER) occurs in the cathodic potentials via the reduction of proton (H^+), and the metal dissolution occurs at anodic potentials via corrosion reactions (e.g., $Fe \rightarrow Fe^{++} + 2e^-$). A lower E_{corr} often signifies greater tendency for the anodic reactions to take place. Corrosion current density, i_{corr}, is a kinetic corrosion property indicating the rate of corrosion reactions (e.g., $Fe \rightarrow Fe^{++} + 2e^-$), therefore a higher i_{corr} is indicative of higher corrosion rate[14].

Furthermore, polarization resistance Rp is calculated by the Stern and Geary[15] equation as given below:

$$i_{corr} = \frac{1}{R_p}\left[\frac{\beta_a.\beta_c}{2.303(\beta_a + \beta_C)}\right]$$

where R_p is the polarization resistance, β_a is the slope in linear anodic region and β_c is the slope in linear cathodic region of the potentiodynamic polarization curve. From **Table 4** it was found the polarization resistance, R_p, for the GI was consistently higher

than GB. The polarization resistance, R_p, is in line with the oxide resistance $R_{(OX)}$ obtained from the EIS for both the GI and GB (See **Table 3**).

Table 4 Corrosion properties extracted from the Tafel fitting of the potentiodynamic polarization of sensitized 304L stainless steel sample.

Region/ Corrosion properties	E_{corr} (V vs. Ag/AgCl)	i_{corr} ($\mu A/cm^2$)	β_a (V/decade)	β_c (V/decade)	R_p ($ohm.cm^2$)
GI	0.279	5.5×10^2	0.339	0.458	153.8
GB	0.121	2.3×10^3	0.461	0.271	32.2

Higher electrochemical activity was exhibited at the GB region than for GI of the sensitized 304L stainless steel from both EIS and potentiodynamic polarization tests. This could be due to the Cr depletion region around the GB structure resulted from the sensitization process. Cr depletion might possibly lead to the formation of relatively less passivating oxide layer, which is revealed by the lower impedance, lower E_{corr}, and higher i_{corr} values of the GB as compared to GI. This indicated that localized electrochemical characterizations are sensitive to reflect the elemental composition (i.e, Cr-depletion) at the grain boundary scale.

3.3 Localized electrochemical characterization of Fe^{++} ion irradiated 304L stainless steel

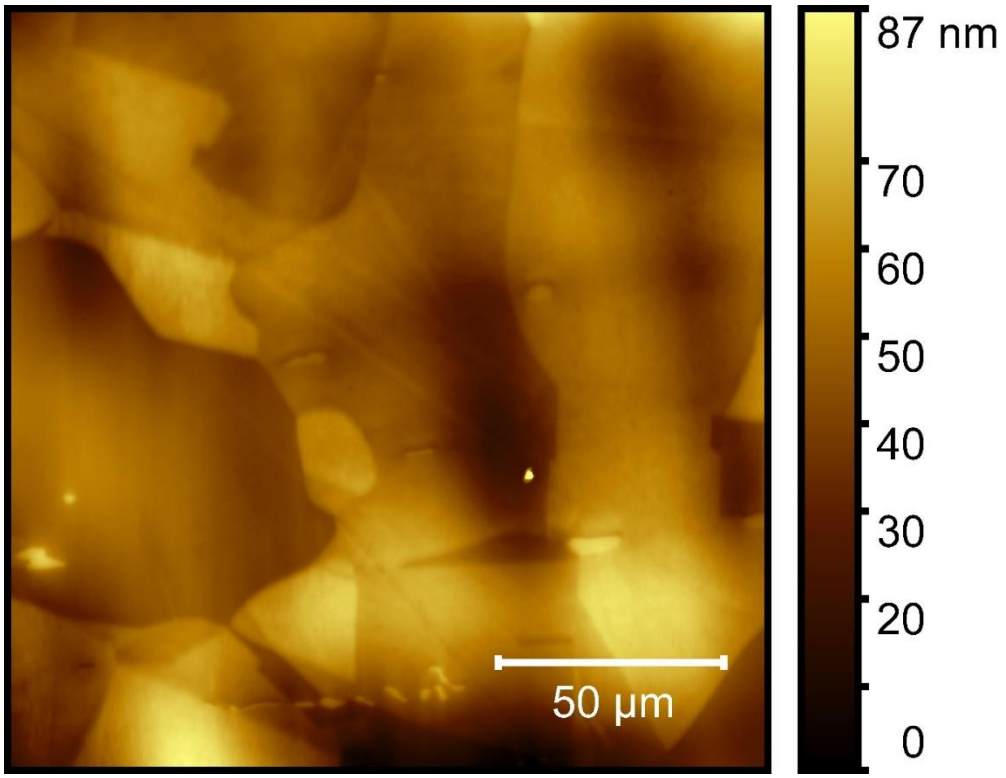

Figure 6. VSI image showing the grains and grain boundaries feature of the Fe^{++} ion irradiated 304L stainless steel sample.

Figure 6 shows the VSI image depicting the microstructure of 304L stainless steel in as irradiated condition. This image reveals the different grains with grain boundaries due to the difference in grain's topographical height.

As the sensitivity of SECM has been demonstrated to resolve corrosion properties of sensitized grain boundaries. The localized electrochemical impedance spectroscopy (EIS) tests were performed on irradiated stainless steel, over grain interior/bulk and over grain boundaries (as shown in **Figure 7**(a & b) and (c)). In line with sensitized 304L, **Figure 7**(d) shows the Nyquist plot of Fe-irradiated 304L, depicting the higher impedance of the GI regions than that of GB. The EIS spectra of GB and GI regions was modeled by using the electrochemical equivalent circuit shown in **Figure 5**. The resulting value of EEC elements is given in

Table *5*. It was observed that the oxide layer over GI exhibited higher resistance compared to that over GB, suggesting irradiation-induced damage accelerates corrosion activities at the GB.

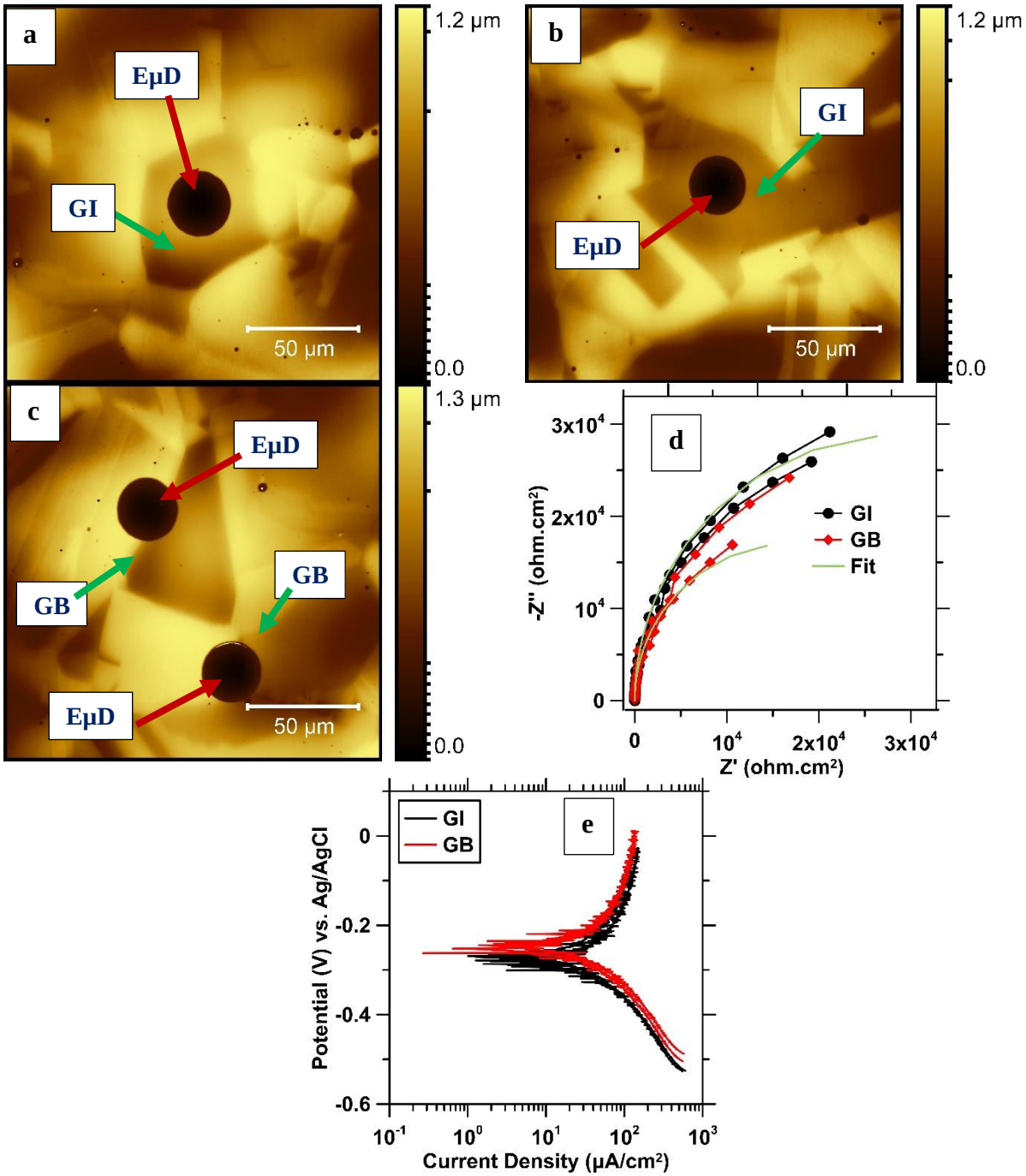

Figure 7. VSI images (a-c) in which the corrosive electrolyte microdroplets (EμDs) are placed over grain interior (GIs) (a & b) and over grain boundaries GBs (c) for electrochemical impedance spectroscopy (EIS) of Fe^{++} ion (5 dpa) irradiated 304L stainless steel.

Table 5 EEC element values from the EIS spectra fitting of GI and GB of Fe^{++} ion irradiated 304L stainless steel.

Region/EEC element	R_s (ohm.cm^2)	$CPE_{(OX)}$-T (Ω^{-1} cm^{-2}s$^{\alpha}$)	$CPE_{(OX)}$-α	$R_{(OX)}$ (ohm.cm^2)
GI	$(0.9 \pm 0.1) \times 10^{-3}$	$3.0 \times 10^{-6} \pm 5.2 \times 10^{-8}$	0.998 ± 0.002	$5.8 \times 10^{4} \pm 2.0 \times 10^{3}$
GB	$(0.7 \pm 0.2) \times 10^{-3}$	$5.5 \times 10^{-6} \pm 1.1 \times 10^{-7}$	0.999 ± 0.002	$3.4 \times 10^{4} \pm 1.4 \times 10^{3}$

Figure 7(e) shows the potentiodynamic polarization plot for the GI and GB regions of the Fe^{++} irradiated 304L stainless steel. **Table 6** listed the corrosion properties such corrosion potential (E_{corr}), corrosion current (i_{corr}), which were obtained from the Tafel fitting of the polarization curves. From **Table 6**,**Table *6*** it was observed that the E_{corr} value of GB (-0.276 ± 0.008 V) is not significantly different as compared to GI (-0.287 ± 0.014 V) region. In addition, the corrosion current density, i_{corr}, of GB (56 ± 0.1 μA/cm^2) was only slightly higher when compared GI (50 ± 4.0 μA/cm^2). However, GI regions exhibit greater values in both oxide resistance $R_{(OX)}$, and polarization resistance, Rp, that are distinctively higher than GB regions. Both the EIS and potentiodynamic polarization tests indicate that irradiated GBs are of slightly higher electrochemical activity when compared to grain interior. This is possibly due to Cr-depletion at the grain boundaries resulting from the ion irradiation assisted elemental segregation. However, as indicated by STEM analysis in **Figure 3**, the extent of Cr-depletion was not as severe as the sensitized grain boundaries, wherein more distinguished corrosion properties were observed at GI and GB regions (see **Figure 4**).

Table 6. Corrosion properties extracted from the Tafel fitting of the potentiodynamic polarization the Fe^{++} ion irradiated 304L stainless steel sample.

Region/ Corrosion properties	E_{corr} (V vs. Ag/AgCl)	i_{corr} (μA/cm^2)	β_a (V/decade)	β_c (V/decade)	R_p (ohm.cm^2)
GI	-0.287 ± 0.014	50 ± 4.0	0.532 ± 0.039	0.249 ± 0.006	1473 ± 55.6
GB	-0.276 ± 0.008	56 ± 0.1	0.608 ± 0.012	0.240 ± 0.005	1334 ± 75.4

3.4 Localized electrochemical characterization of Ni^{++} ion irradiated and strained 316L stainless steel

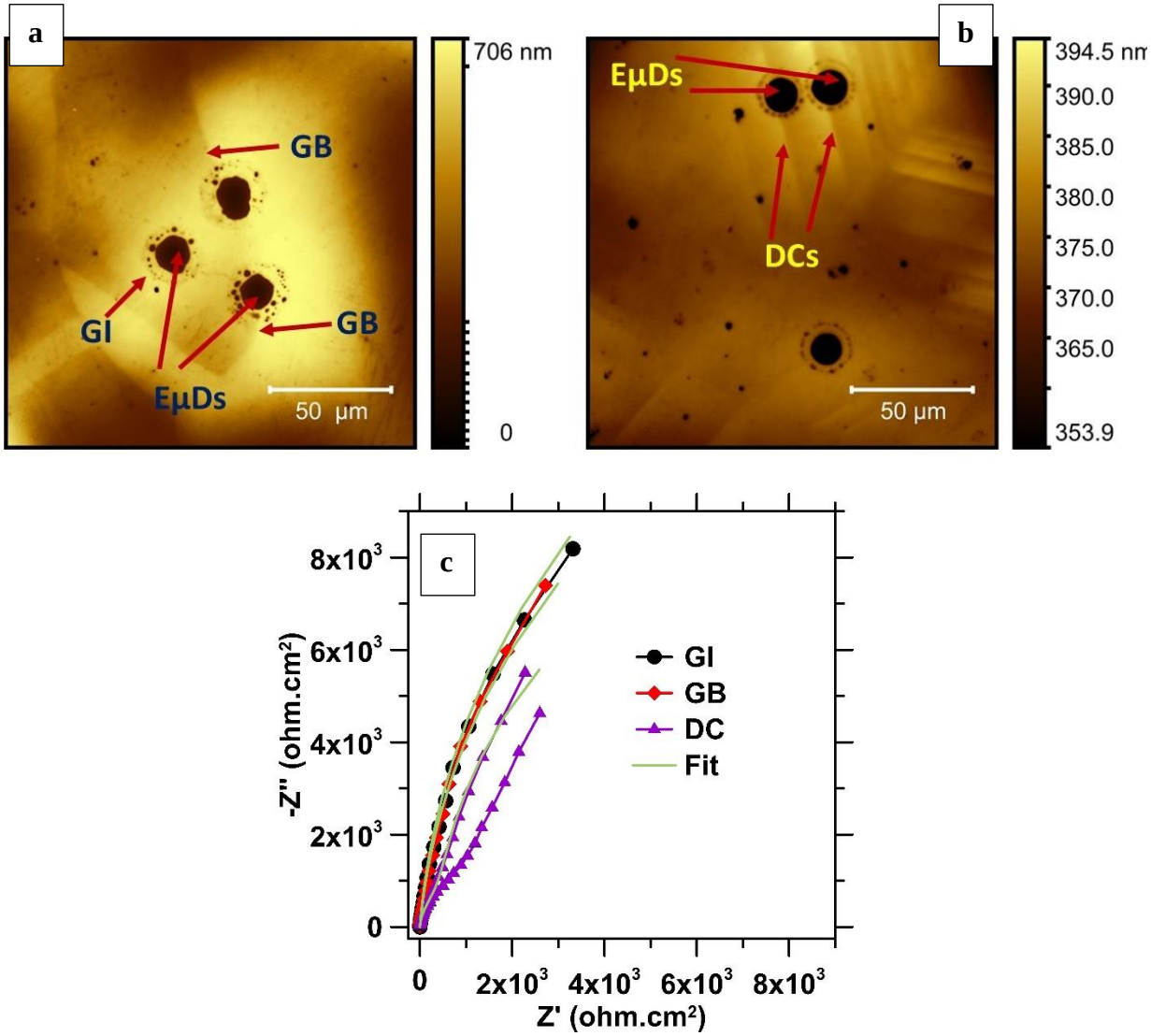

Figure 8 VSI images in which the corrosive electrolyte microdroplets (EμDs) are placed (a) over grain interiors (GIs) and grain boundaries (GBs) and (c) over dislocation channels (DCs) for electrochemical impedance spectroscopy (EIS) of Ni^{++} ion (2 dpa) irradiated and strained to fractured 316L stainless steel.

Despite irradiated grain boundaries were not significantly corrosion-susceptible as compared to sensitized grain boundaries, we progressed our study to resolve localized corrosion in irradiated and deformed stainless steel. In a Ni-irradiated (2 dpa), strained-to-fractured 316L sample, VSI images show the grain interior (GI) & grain boundary (GB) structure (**Figure 8**(a)) and the dislocation channels (DC) induced by mechanical strain (**Figure 8**(b)). Microprobes were located at the microstructural features to conduct localized electrochemical measurements. **Figure 8**(c) illustrates the Nyquist plot acquired from the EIS test. It is depicted by **Figure 8**(c) that DC exhibited lowest impedance than other microstructural features. From equivalent circuit fitting (shown in **Figure 5**) of EIS results (given in **Table 7**), it is evident that the electrochemical activity

increased in the order GI < GB < DC, wherein the difference between GI and GB is not significant. But the great decrease in DC's corrosion resistance signifying higher corrosion susceptibility that is consistent with our previous reports.

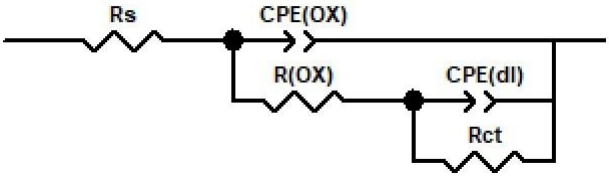

Figure 9 Electrochemical equivalent circuit used for modelling the EIS spectra over DC.

Table 7 EEC element values from the EIS spectra fitting of GI, GB, & DC of Ni^{++} ion irradiated and strained 304L stainless steel.

Region/EEC element	GI	GB	DC
R_s (ohm.cm^2)	$(1.0 \pm 0.3) \times 10^{-1}$	$(8.5 \pm 3.0) \times 10^{-2}$	$(1.5 \pm 0.3) \times 10^{-1}$
$CPE_{(OX)}$-T (Ω^{-1} cm^{-2}s$^{\alpha}$)	$1.8\times10^{-5} \pm 2.1\times10^{-7}$	$2.1\times10^{-5} \pm 2.6\times10^{-7}$	$1.6\times10^{-5} \pm 3.6\times10^{-7}$
$CPE_{(OX)}$-α	0.948 ± 0.002	0.941 ± 0.002	0.949 ± 0.003
$R_{(OX)}$ (ohm.cm^2)	$3.2\times10^{4} \pm 1.8\times10^{3}$	$2.8\times10^{4} \pm 1.8\times10^{3}$	$2.0\times10^{3} \pm 1.0\times10^{2}$
$CPE_{(dl)}$-T (Ω^{-1} cm^{-2}s$^{\alpha}$)	-	-	$1.2\times10^{-5} \pm 3.5\times10^{-7}$
$CPE_{(dl)}$-α	-	-	0.999 ± 0.001
$R_{(ct)}$ (ohm.cm^2)	-	-	$1.7\times10^{4} \pm 9.9\times10^{3}$

4. Conclusions

The scanning electrochemical cell microscopy has been successfully utilized to reveal the difference in the electrochemical activity caused by the (ion) irradiation assisted elemental segregation and mechanical deformation. Herein, the localized electrochemical tests revealed the higher electrochemical activity at the GB than that for GI for the sensitized, ion-irradiated, and ion-irradiated and mechanically-strained stainless steels. These results demonstrated the grain-boundary sensitivity of the electrochemical scanning probe techniques, which can be employed to detect IASCC susceptibility in irradiated and deformed nuclear components.

Future Work

1. Localized electrochemical characterizations and TEM/STEM study at the intersection of dislocation channel and grain boundary.
2. Oxidation of irradiated and deformed stainless steel in reactor-relevant conditions.
3. Localized scanning probe characterization and TEM/STEM study of the irradiated, oxidized, and deformed stainless steels.

References

(1) Was, G. S.; Busby, J. T. Role of Irradiated Microstructure and Microchemistry in Irradiation-Assisted Stress Corrosion Cracking. *Philosophical Magazine* **2005**, *85* (4–7), 443–465. https://doi.org/10.1080/02678370412331320224.

(2) Kuang, W.; Hesterberg, J.; Was, G. S. The Effect of Post-Irradiation Annealing on the Stress Corrosion Crack Growth Rate of Neutron-Irradiated 304L Stainless Steel in Boiling Water Reactor Environment. *Corrosion Science* **2019**, *161*, 108183. https://doi.org/10.1016/j.corsci.2019.108183.

(3) Deng, P.; Peng, Q.; Han, E.-H.; Ke, W.; Sun, C. Proton Irradiation Assisted Localized Corrosion and Stress Corrosion Cracking in 304 Nuclear Grade Stainless Steel in Simulated Primary PWR Water. *Journal of Materials Science & Technology* **2021**, *65*, 61–71. https://doi.org/10.1016/j.jmst.2020.04.068.

(4) Was, G. S.; Farkas, D.; Robertson, I. M. Micromechanics of Dislocation Channeling in Intergranular Stress Corrosion Crack Nucleation. *Current Opinion in Solid State and Materials Science* **2012**, *16* (3), 134–142. https://doi.org/10.1016/j.cossms.2012.03.003.

(5) Rajan, P. B. R.; Monnet, I.; Hug, E.; Etienne, A.; Enikeev, N.; Keller, C.; Sauvage, X.; Valiev, R.; Radiguet, B. Irradiation Resistance of a Nanostructured 316 Austenitic Stainless Steel. *IOP Conf. Ser.: Mater. Sci. Eng.* **2014**, *63* (1), 012121. https://doi.org/10.1088/1757-899X/63/1/012121.

(6) FUKUYA, K.; NAKANO, M.; FUJII, K.; TORIMARU, T. Role of Radiation-Induced Grain Boundary Segregation in Irradiation Assisted Stress Corrosion Cracking. *Journal of Nuclear Science and Technology* **2004**, *41* (5), 594–600. https://doi.org/10.1080/18811248.2004.9715522.

(7) Porter, D. L. Ferrite Formation in Neutron-Irradiated Type 304L Stainless Steel. *Journal of Nuclear Materials* **1979**, *79* (2), 406–411. https://doi.org/10.1016/0022-3115(79)90105-3.

(8) Stanley, J. T.; Hendrickson, L. E. Ferrite Formation in Neutron-Irradiated Austenitic Stainless Steel. *Journal of Nuclear Materials* **1979**, *80* (1), 69–78. https://doi.org/10.1016/0022-3115(79)90221-6.

(9) Boisson, M.; Legras, L.; Andrieu, E.; Laffont, L. Role of Irradiation and Irradiation Defects on the Oxidation First Stages of a 316L Austenitic Stainless Steel. *Corrosion Science* **2019**, *161*, 108194. https://doi.org/10.1016/j.corsci.2019.108194.

(10) TERACHI, T.; FUJII, K.; ARIOKA, K. Microstructural Characterization of SCC Crack Tip and Oxide Film for SUS 316 Stainless Steel in Simulated PWR Primary Water at 320°C. *Journal of Nuclear Science and Technology* **2005**, *42* (2), 225–232. https://doi.org/10.1080/18811248.2005.9726383.
(11) Sowa, M.; Simka, W. Electrochemical Impedance and Polarization Corrosion Studies of Tantalum Surface Modified by DC Plasma Electrolytic Oxidation. *Materials* **2018**, *11* (4), 545. https://doi.org/10.3390/ma11040545.
(12) Láng, G.; Heusler, K. E. Remarks on the Energetics of Interfaces Exhibiting Constant Phase Element Behaviour. *Journal of Electroanalytical Chemistry* **1998**, *457* (1), 257–260. https://doi.org/10.1016/S0022-0728(98)00301-5.
(13) Chung, S. C.; Cheng, J. R.; Chiou, S. D.; Shih, H. C. EIS Behavior of Anodized Zinc in Chloride Environments. *Corrosion Science* **2000**, *42* (7), 1249–1268. https://doi.org/10.1016/S0010-938X(99)00129-8.
(14) Papavinasam, S. 3 - Electrochemical Polarization Techniques for Corrosion Monitoring. In *Techniques for Corrosion Monitoring (Second Edition)*; Yang, L., Ed.; Woodhead Publishing Series in Metals and Surface Engineering; Woodhead Publishing, 2021; pp 45–77. https://doi.org/10.1016/B978-0-08-103003-5.00003-5.
(15) Stern, M.; Geary, A. L. Electrochemical Polarization: I . A Theoretical Analysis of the Shape of Polarization Curves. *J. Electrochem. Soc.* **1957**, *104* (1), 56. https://doi.org/10.1149/1.2428496.
(16) Gaillard, N.; Gros-Jean, M.; Mariolle, D.; Bertin, F.; Bsiesy, A. Method to Assess the Grain Crystallographic Orientation with a Submicronic Spatial Resolution Using Kelvin Probe Force Microscope. *Applied Physics Letters* **2006**, *89* (15), 154101. https://doi.org/10.1063/1.2359297.
(17) Hua, Z.; An, B.; Iijima, T.; Gu, C.; Zheng, J. The Finding of Crystallographic Orientation Dependence of Hydrogen Diffusion in Austenitic Stainless Steel by Scanning Kelvin Probe Force Microscopy. *Scripta Materialia* **2017**, *131*, 47–50. https://doi.org/10.1016/j.scriptamat.2017.01.003.
(18) Jiang, B.; Guo, T.; Peng, Q.; Jiao, Z.; Volinsky, A. A.; Gao, L.; Ma, Y.; Qiao, L. Proton Irradiation Effects on the Electron Work Function, Corrosion and Hardness of Austenitic Stainless Steel Phases. *Corrosion Science* **2019**, *157*, 498–507. https://doi.org/10.1016/j.corsci.2019.06.011.